Structural Engineering and Mechanics, Vol. 42, No. 2 (2012) 153-174
DOI: http://dx.doi.org/10.12989/sem.2012.42.2.153

Parameter calibrations and application of micromechanical fracture models of structural steels

Fangfang Liao[2], Wei Wang*[1,2] and Yiyi Chen[1,2]

[1]*State Key Laboratory of Disaster Reduction in Civil Engineering, Tongji University, Shanghai 200092, China*
[2]*Department of Structural Engineering, Tongji University, Shanghai 200092, China*

(Received May 27, 2011, Revised March 9, 2012, Accepted March 10, 2012)

Abstract. Micromechanical facture models can be used to predict ductile fracture in steel structures. In order to calibrate the parameters in the micromechanical models for the largely used Q345 steel in China, uniaxial tensile tests, smooth notched tensile tests, cyclic notched bar tests, scanning electron microscope tests and finite element analyses were conducted in this paper. The test specimens were made from base metal, deposit metal and heat affected zone of Q345 steel to investigate crack initiation in welded steel connections. The calibrated parameters for the three different locations of Q345 steel were compared with that of the other seven varieties of structural steels. It indicates that the toughness index parameters in the stress modified critical strain (SMCS) model and the void growth model (VGM) are connected with ductility of the material but have no correlation with the yield strength, ultimate strength or the ratio of ultimate strength to yield strength. While the damage degraded parameters in the degraded significant plastic strain (DSPS) model and the cyclic void growth model (CVGM) and the characteristic length parameter are irrelevant with any properties of the material. The results of this paper can be applied to predict ductile fracture in welded steel connections.

Keywords: ductile fracture; micromechanical fracture model; parameter calibration; ultra low cycle fatigue; structural steel

1. Introduction

Fracture is a significant failure mode in building structures. Recently, collapse of whole building structures due to connection fracture often occurred. These events not only resulted in casualties, but also caused large economic losses, thus much attention has been paid into this field. Current researches mainly use the conventional fracture mechanics methods, such as the stress intensity factor, crack tip opening displacement (CTOD) and J integral. Since they all assume that crack already exists and there is high strain constraint in the initial crack tip, they are suitable to study brittle fracture with limited plasticity, but not applicable to investigate ductile fracture with large scale yielding region and no initial flaw under low cyclic loading. In addition, the conventional fracture mechanics methods do not take triaxiality into consideration, so they are not fit for fracture prediction of connections controlled by triaxial stress condition.

*Corresponding author, Associate Professor, E-mail: weiwang@tongji.edu.cn

Earthquake-induced fractures are always characterized by large-strain low-cycle conditions. Cyclic loading due to earthquakes typically involves less than ten cycles and strains that are in well excess of yield. Such conditions are defined as ultra low cycle fatigue (ULCF) which could not be predicted by traditional fracture mechanics methods. Previous studies (Stojadinovic *et al*. 2000, Kuroda 2002, Tateishi and Hanji 2004, Chen 2007, Tateishi *et al*. 2007) have made some efforts to study the ULCF strength of structural steels and welded joints. Micromechanics-based facture models aim to seize the fundamental fracture initiation mechanisms of void nucleation, growth and coalescence. They can capture the effect of stress and strain state on fracture prediction. Hancock and Cowling (1980) recognized that ductile fracture is not only related to the state of the strains but also that of the triaxial stresses, so they employed the concept of a failure locus curve i.e. fracture strain VS. triaxiality which was later used by Theocaris (1995). The micromechanical models of various stages of ductile fracture are presented by Benzerga and Leblond (2010). In their work, cup-cone and slant fracture were simulated, macroscopic plastic flow localization was analyzed, and quantitative prediction of fracture in notched bars and crack growth simulation were conducted. The void growth model (VGM) is based on research by Rice and Tracey (1969), while the stress modified critical strain (SMCS) model is based on research by Hancock and Mackenzie (1976), and then further investigated by Panontin and Sheppard (1995). They have been verified to accurately predict ductile fracture in steel connection details under monotonic loading through a series of twelve pull-plate experiments and complementary finite-element analyses of bolted connections and Reduced Beam Section type details (Kanvinde and Deierlein 2006, 2007a). The degraded significant plastic strain (DSPS) model and the cyclic void growth model (CVGM) aim to capture ULCF behavior and they have been validated to predict ULCF in steel through a series of tests and analyses of fourteen blunt notch specimens and four dog bone specimens (Kanvinde and Deierlein 2007b, 2008). Micromechanics-based models were used to investigate ULCF in large-scale steel bracing members in special concentrically braced frame systems (Fell and Myers 2006). Later, the results of six large-scale tests on column base plate connections subjected to cyclic loading demonstrate the ability of the CVGM to predict fracture initiation in realistic steel connection details (Myers *et al.* 2009).

However, former researches on the application of micromechanical models are mainly for base metal and steel brace, there isn't much study on their application into fracture prediction of welded connections especially welded steel tubular connections which are largely used in large span steel structures. In order to extend the use of these micromechanical models to predict ductile fracture in welded steel connections in China, material tests, scanning electron microscope tests and finite element analyses were conducted in this paper to calibrate the parameters in these models for popularly used Q345 steel in China. Q345 steel is a kind of low-alloy steel, the average carbon content of which is 0.16%, and the main alloying elements are manganese, silicon, sulphur, phosphorus, vanadium, niobium, titanium etc.. Its nominal yield strength is 345 N/mm^2, and it is widely used in steel structures in China. The test specimens were made from base metal, deposit metal and heat affected zone to investigate the crack initiation.

2. Scope and objectives

This paper begins with a brief overview of theories of micromechanics-based models, and then presents four kinds of calibration tests. Nine uniaxial tensile tests of round bars made of Q345 base

metal, deposit metal and heat affected zone were conducted to provide stress-strain data, elastic modulus, strength and ductility which were needed in finite element analyses. Eighteen tensile tests of circumferentially smooth-notched bars and corresponding finite element analyses were carried out to calibrate the parameters of the SMCS and the VGM models. Thirty-six cyclic tests of circumferentially smooth-notched bars and their finite element analyses were done for calibrating the DSPS and CVGM models. The fracture surfaces of nine notched tensile specimens were scanned to calibrate the characteristic lengths of the three materials. Subsequently, the calibrated parameters for the three different locations of Q345 steel were compared with that of the other seven previously calibrated structural steels to study the relationships of the parameters with the properties of the material. Finally, the application of calibrated micromechanical fracture models to welded steel connection is given.

3. Theories of micromechanics-based models

Micromechanics-based models attribute ductile fracture to void nucleation, growth and coalescence. These models capture the combined effects of the triaxiality and plastic strain on void growth that results in crack initiation. SMCS and VGM models are used to predict fracture initiation under monotonic loading, while DSPS and CVGM models are fit for fracture prediction under ULCF loading. Due to Rice and Tracey's VGM model, fracture is predicted to occur when an integral of stress and strain history is equal to a critical value η. This corresponds to the voids growing large enough to exceed a critical void size to trigger necking instabilities between voids causing coalescence and crack formation. Mathematically, VGM criterion can be expressed as follows

$$\int_0^{\varepsilon_p^{critical}} \exp(1.5\sigma_m/\sigma_e)\cdot d\varepsilon_p - \eta > 0 \tag{1}$$

where σ_m and σ_e are mean and effective stress respectively, $T = \sigma_m/\sigma_e$ is stress triaxiality, $d\varepsilon_p$ is differential increment of the equivalent plastic strain ε_p, and η is a material parameter that quantifies the critical void ratio. In addition, η is a material property that is constant for a specific material and it increases with material toughness. η can be determined by calibration of notched round bar tensile tests that will be described in detail in the following sections.

VGM model Eq. (1) includes an explicit term for integrating the triaxiality with respect to plastic strain. However in many realistic situations, the triaxiality remains relatively constant during the loading history. Therefore, the terms inside the integral in Eq. (1) can be represented as a product that underlies the SMCS criterion expressed as follows

$$\varepsilon_p - \alpha\exp(-1.5\sigma_m/\sigma_e) > 0 \tag{2}$$

where the toughness index α is a material constant that can be determined through notched round bar tensile tests, just like the parameter η in the VGM.

In ULCF situation, according to CVGM model, the tensile cycles correspond to void growth and the compressive cycles correspond to void shrinkage, when the void size reaches its critical value, fracture can be predicted to occur. While under cyclic loading, the critical void size is degraded as

compared to that under monotonic loading because of the accumulated damage. Using an exponential function as damage function, CVGM model can be expressed as follows

$$\exp(-\lambda_{CVGM}\varepsilon_p)\cdot\eta_{monotonic} = \sum_{tensile-cycles}\int_{\varepsilon_1}^{\varepsilon_2}\exp(|1.5T|)\cdot d\varepsilon_t - \sum_{compressive-cycles}\int_{\varepsilon_1}^{\varepsilon_2}\exp(|1.5T|)\cdot d\varepsilon_c \quad (3)$$

where ε_p is the equivalent plastic strain at the beginning of the last tensile cycle, it denotes damage variable, $\eta_{monotonic}$ is the toughness parameter of the material under monotonic loading, λ_{CVGM} is the damage degraded parameter of the material under cyclic loading which can be calibrated through cyclic tests of notched round bars, corresponding finite element analyses and curve fit of scatter plot, the detailed calibration process is presented later. The term on the left hand side of Eq. (3) denotes the critical void size under cyclic loading, while the terms on the right hand side of Eq. (3) denote the cumulative results of void growth during all the tensile cycles and void shrinkage during all the compressive cycles. When the value of the right hand side of Eq. (3) exceeds that of the left hand side, crack initiation can be predicted to occur.

Similar to SMCS model, DSPS model also assumes that the triaxiality keeps constant during the loading history, therefore the terms inside the integral in Eq. (3) can be represented as a product, in the meantime, significant plastic strain is denoted as $\varepsilon^* = \varepsilon_t - \varepsilon_c$ (i.e., the difference between the cumulative tensile strain and the cumulative compressive strain), then the DSPS model can be expressed as follows

$$\varepsilon^*_{critical} = \exp(-\lambda_{DSPS}\varepsilon_p)\cdot\varepsilon_p^{critical} \quad (4)$$

where $\varepsilon_p^{critical}$ is the critical equivalent plastic strain under monotonic loading, damage degraded parameter λ_{DSPS} is similar to λ_{CVGM} in the CVGM model which can be calibrated through cyclic tests of notched round bars, corresponding finite element analyses and curve fit of scatter plot.

In the above micromechanical models, ductile crack initiation is not the behavior of a single material point but that of a critical volume of material. Therefore, it is necessary to define a characteristic length parameter l^* that includes several material points. Micromechanical models must be satisfied over the characteristic length l^* to trigger ductile crack initiation. The value of l^* depends on the microstructure of the material and can be obtained from scanning electron micrographs. Currently, the proposed approach to determine characteristic length l^* is to have two bounds and a most likely value. The lower bound is twice the average dimple diameter, the upper bound is the length of the largest plateau or trough observed in the angled fractograph, and the mean value of l^* can be arrived at by taking an average over roughly ten measurements of the lengths of the plateaus and troughs. This would be the most likely estimate of the l^* value.

4. Tests and analyses for parameter calibrations of Q345 steel

4.1 Welding process and specimen manufacture

Two Q345 steel plates with thickness of 40 mm were connected with full penetration welding shown in Fig. 1. One steel plate was grooved to angle 45°, and carbon-dioxide arc welding was used. Base plate was added, welding wire was Atlantic CHW50C8, and the diameter was 1.2 mm.

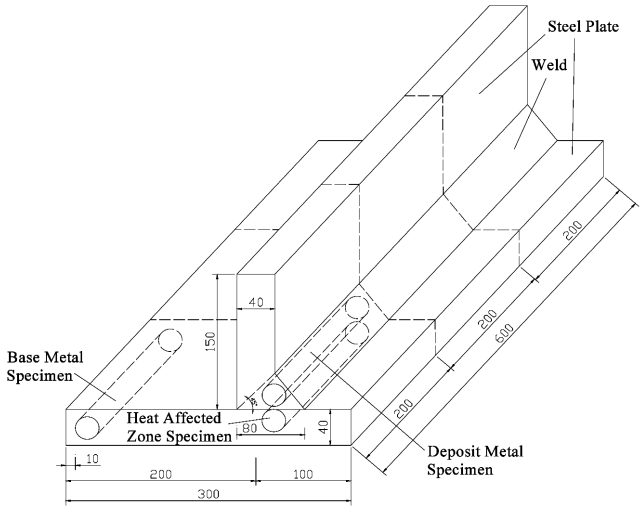

Fig. 1 *T* welded steel plate connection specimen

The weld was detected with UT and the quality of the weld belongs to the first grade. Seven specimens shown in Fig. 1 were manufactured (three base metal round bars, three deposit metal round bars and three heat affected zone round bars can be extracted from each specimen). After being manufactured, the specimens were cut into three equal parts to facilitate the extraction of round bars. Round bar specimens were used to do uniaxial tensile tests, smooth-notched tensile tests and cyclic notched bar tests.

4.2 Uniaxial tensile tests

Three base metal round bars, three deposit metal round bars and three heat affected zone round bars were extracted from the *T* welded steel plate connections and then manufactured to the dimension shown in Fig. 2. These nine specimens were used to carry out uniaxial tensile tests. Serial numbers and measured dimensions of the specimens can be seen in Table 1. The gage length of the extensometer is 50 mm. The stress-strain curves, the yield strength σ_y, ultimate strength σ_u, and elastic modulus E of the three materials were obtained. The results are shown in Table 2.

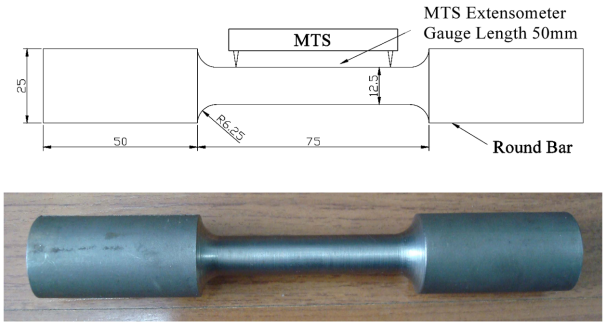

Fig. 2 Round bar tensile specimen

Table 1 Serial numbers and measured dimensions of the uniaxial tensile specimens

Material	No.	Diameter of clamping part (mm)	Diameter of gage length part (mm)	Clamping length (mm)	Middle length (mm)
Base metal	1-1	24.94	12.52	55.60	74.62
	2-1	25.03	12.58	55.44	74.62
	3-1	25.01	12.54	55.25	73.71
Deposit metal	1-2	24.90	12.56	55.09	74.40
	2-2	24.96	12.41	50.03	75.95
	3-2	25.01	12.56	54.83	74.82
Heat affected zone	1-3	25.01	12.48	54.52	74.71
	2-3	24.95	12.27	55.14	75.05
	3-3	25.25	12.38	56.23	73.73

Table 2 Results of the uniaxial tensile tests

Material	No.	σ_y (MPa)	σ_u (MPa)	E (MPa)
Base metal	1-1	323.9	526.6	205000
	2-1	317.0	519.8	216000
	3-1	321.4	522.2	203000
	Mean value	320.8	522.9	208000
Deposit metal	1-2	364.4	477.6	202000
	2-2	391.4	503.7	210000
	3-2	384.4	492.5	209000
	Mean value	380.1	491.3	207000
Heat affected zone	1-3	354.5	520.4	213000
	2-3	360.3	520.0	199000
	3-3	361.2	520.3	170000
	Mean value	358.7	520.2	194000

At some point during the loading process, the specimen starts to neck unstably. At this point, the reading of the extensometer becomes useless because the straining across the extensometer gage length is concentrated in the necking region and no longer uniform. The extensometer was removed at this point to protect it from damage. The test data can only give the stress and strain of the three materials before removing extensometer, while actually the materials can sustain large deformation after removing extensometer and before fracture. Therefore, the true stress-plastic strain curves of the materials used in ABAQUS finite-element analyses should be extended to fracture occurrence. The fracture diameter and the breaking force of the specimens were measured to calculate the true stress and strain at the fracture point (see Table 3). The Eqs. (5) and (6) were used

Table 3 True fracture stress and strain of the uniaxial tensile specimens

Material	No.	Diameter of gage length part d_0 (mm)	Fracture diameter d_f (mm)	Breaking force $F_{fracture}$ (kN)	$\sigma_{true}^{fracture}$	$\varepsilon_{true}^{fracture}$
Base metal	1-1	12.52	6.45	40.73	1247.05	1.33
	2-1	12.58	6.43	39.38	1213.19	1.34
	3-1	12.54	6.45	39.63	1213.43	1.33
	Mean value				1224.55	1.33
Deposit metal	1-2	12.56	6.41	38.21	1184.72	1.35
	2-2	12.41	6.40	-	-	1.32
	3-2	12.56	6.51	38.33	1152.12	1.31
	Mean value				1168.42	1.33
Heat affected zone	1-3	12.48	6.45	39.63	1213.36	1.32
	2-3	12.27	6.48	37.91	1150.01	1.28
	3-3	12.38	6.46	39.15	1195.20	1.30
	Mean value				1186.19	1.30

$$\varepsilon_{true}^{fracture} = \ln[(d_o/d_f)^2] \tag{5}$$

$$\sigma_{true}^{fracture} = \frac{F_{fracture}}{\pi d_f^2/4} \tag{6}$$

where d_0 is the initial diameter of gage length part, and d_f is the fracture diameter of gage length part measured after the test was completed. The true stress-plastic strain curves for the three materials were extended to the fracture point from the point when removing the extensometer by a straight line as shown in Fig. 3. It must be noted that at the point of fracture, the stress and strain distributions across the necked cross section are not uniform, so it is useful to match the load displacement curves from finite element analyses (FEA) to the actual specimens. In this study, the material properties given by Fig. 3 can make the load displacement curves from FEA match well to that of the test specimens. Thus, the curves shown in Fig. 3 were used as material properties in the ABAQUS analyses of smooth notched tensile test specimens.

4.3 Smooth notched tensile tests

The α parameter in the SMCS or the η parameter in the VGM of the three materials was obtained through testing and finite element analyses of circumferentially smooth-notched tensile specimens (e.g., Fig. 4). Each material took three notched radii that were 1.5 mm, 3.125 mm and 6.25 mm to provide varied triaxiality condition. Since the contours of the SMCS or VGM fields are very flat across the cross section of the notched round bars, ductile fracture initiation in these specimens appears to take place almost simultaneously over most of the central part of the bar cross section. This strong dependence of the failure on the α or the η as opposed to the characteristic length l^* makes the smooth notched tensile tests suitable for calibrating α or η. The design dimension of

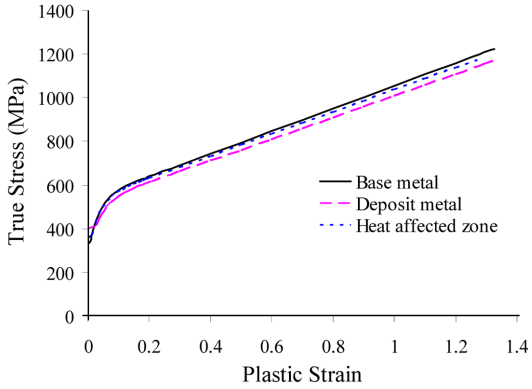

Fig. 3 True stress-plastic strain curves

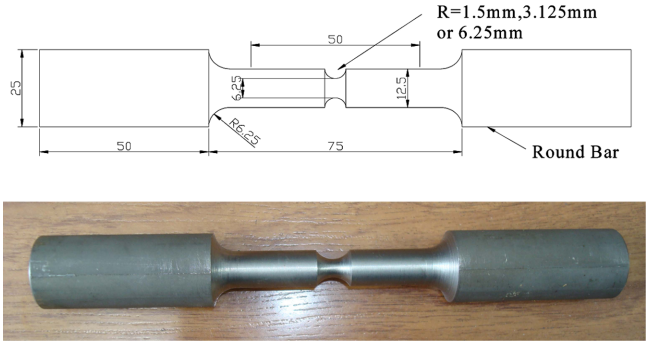

Fig. 4 Smooth notched tensile test specimens

each specimen can be seen in Fig. 4. Each kind of specimens was manufactured with the quantity of two. Serial numbers and measured dimensions of the specimens can be seen in Table 4. The grips, extensometer and loading apparatus are the same as in the uniaxial tensile specimens.

The point with sudden change in the slope of the force versus elongation curve corresponds to the initiation of ductile fracture. This displacement is used as the controlling displacement in the companion finite element analyses to back calculate the fracture parameters α and η. Since the extensometer was removed before the fracture point for the uniaxial tensile specimens, the experimental displacement corresponding to fracture that must be used in the companion finite element analyses could not be obtained. Therefore, the uniaxial tensile tests of un-notched specimens could not be used to calibrate the parameters α and η.

Elastic-plastic finite element analyses for the notched tensile specimens were conducted using ABAQUS/CAE 6.10. Nonlinear, large-deformation plasticity models were used. The models employed incremental plasticity with a von Mises yield surface and isotropic strain hardening. The material property was a piece-wise linear fit to the measured true stress-plastic strain curve obtained from uniaxial tensile tests (shown in Fig. 3). Two-dimensional, axisymmetric finite element analyses with element type of CAX8R were performed. As shown in Fig. 5, the element size was refined to about 0.25 mm in the notch area, which is sufficient to capture the stress-strain gradients in that area (Chi 2000) and is comparable to the characteristic length l^* as listed in Table 8. The FEM contained

Table 4 Serial numbers and measured dimensions of the notched tensile specimens

Material	Notch size (mm)	No.	Diameter of clamping part (mm)	Diameter of gage length part (mm)	Clamping length (mm)	Middle length (mm)	Diameter of notched part (mm)
Base metal	1.5	4-1	24.94	12.50	54.86	74.85	6.26
		5-1	24.93	12.49	51.18	75.24	6.24
	3.125	10-1	25.00	12.53	55.10	75.15	6.22
		11-1	24.95	12.63	54.67	74.84	6.20
	6.25	16-1	24.93	12.54	54.81	75.25	6.36
		17-1	24.84	12.54	54.82	75.00	6.27
Deposit metal	1.5	4-2	25.02	12.54	55.38	74.81	6.17
		5-2	24.77	12.54	54.87	74.95	6.24
	3.125	10-2	25.02	12.56	54.33	74.88	6.30
		11-2	24.90	12.55	55.12	74.86	6.34
	6.25	16-2	24.99	12.53	55.03	75.20	6.20
		17-2	24.90	12.52	55.04	75.15	6.33
Heat affected zone	1.5	4-3	25.04	12.53	55.35	74.98	6.19
		5-3	24.80	12.48	55.23	74.77	6.24
	3.125	10-3	24.93	12.57	54.91	74.62	6.29
		11-3	25.07	12.56	55.40	74.22	6.28
	6.25	16-3	25.00	12.55	54.55	75.89	6.26
		17-3	24.91	12.57	55.88	74.86	6.27

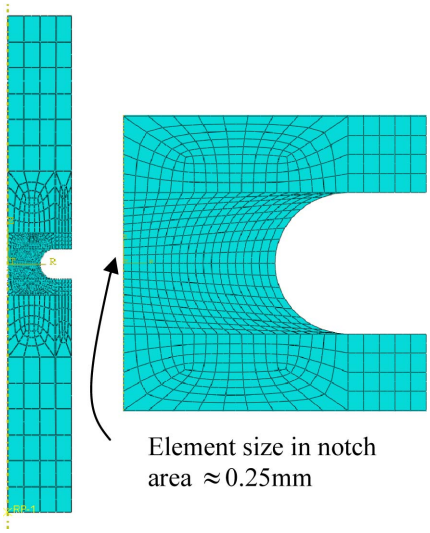

Fig. 5 Axisymmetric finite element model of notched tensile specimen ($R = 1.5$ mm)

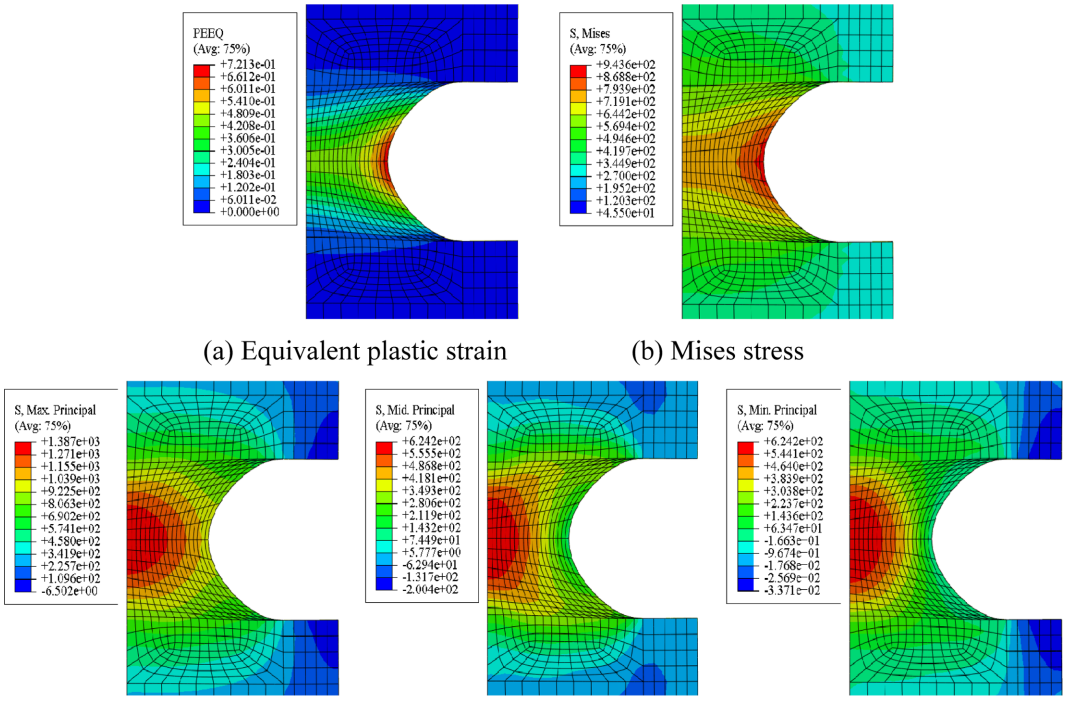

(a) Equivalent plastic strain (b) Mises stress

(c) Maximum principal stress (d) Middle principal stress (e) Minimum principal stress

Fig. 6 Strain and stress fields in notch area (specimen 4-1)

nearly 800, 1350, 1650 elements for specimens with $R = 1.5$ mm, 3.125 mm or 6.25 mm respectively. The strain and stress fields are very flat over the most critical section of the specimens as shown in Fig. 6. Fig. 7 gives the comparison of finite element analyses and test data for force elongation curves for all the three geometries of the three materials. It can be seen that the FEA curves are very close to the test curves, and similar agreement is observed for all the other specimens as well.

The critical value of the SMCS model parameter α was determined from the testing and analyses of notched tensile specimens with varying notch severity. The tensile tests were conducted to identify the displacement corresponding to fracture initiation. Finite element analyses of each notched tensile geometry were performed to obtain the stresses and strains at the displacement corresponding to fracture initiation. Substituting these critical stress and strain states at the cross section into the SMCS criterion to enforce a zero value at the section center determined the fracture parameter α

$$\alpha = \varepsilon_p^{critical} \exp(1.5T) = \varepsilon_p^{critical} \exp(1.5\sigma_m/\sigma_e) \tag{7}$$

The calibration process for the η parameter of the VGM is similar to that of the SMCS, however, some of the mathematical expressions used are different. The η for a given test can be calculated by evaluating the following Eq. (8) at the point of failure. The calculation results of parameters α and η are shown in Table 5.

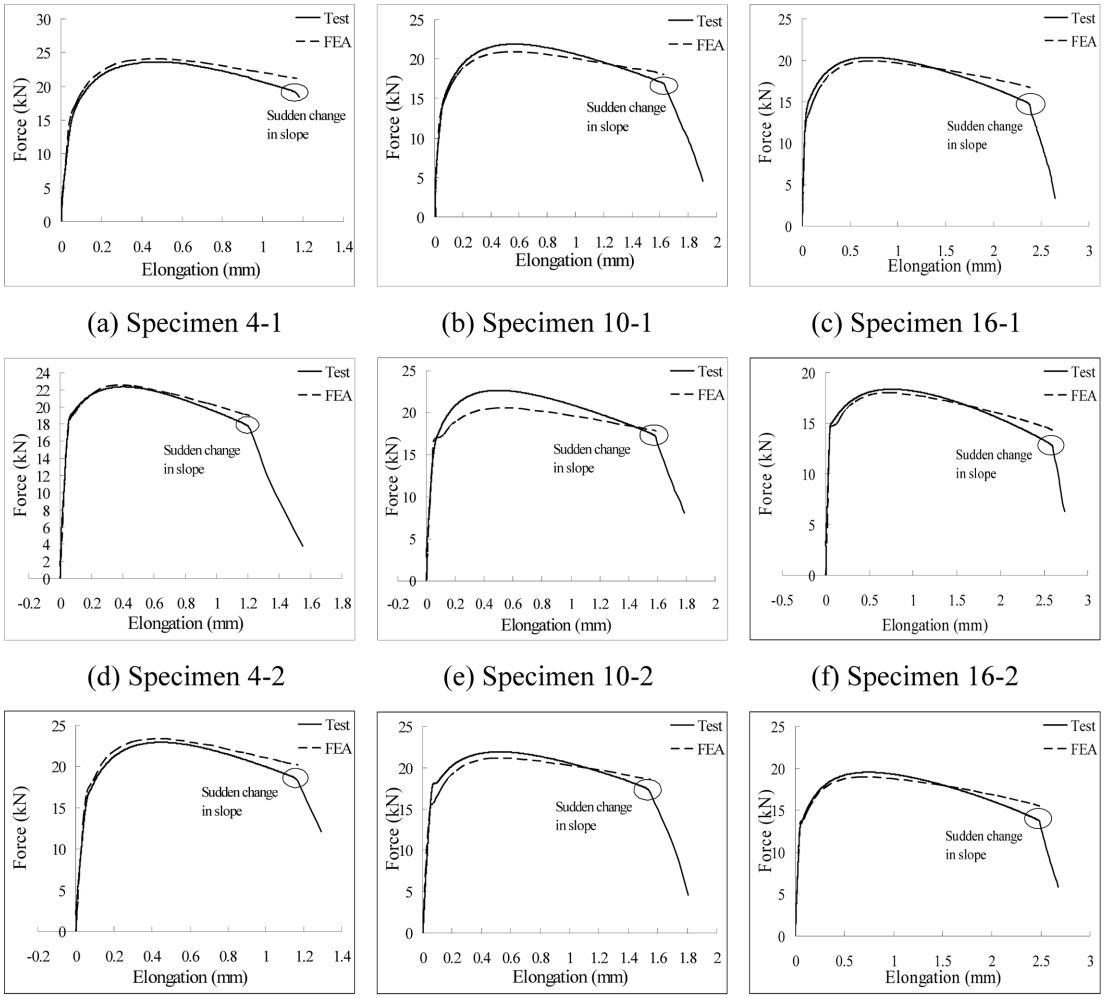

(a) Specimen 4-1 (b) Specimen 10-1 (c) Specimen 16-1

(d) Specimen 4-2 (e) Specimen 10-2 (f) Specimen 16-2

(g) Specimen 4-3 (h) Specimen 10-3 (i) Specimen 16-3

Fig. 7 Comparison of FEA and test data for force elongation curves for smooth notched tensile specimens

$$\eta = \int_0^{\varepsilon_p} \exp(1.5T) \cdot d\varepsilon_p \tag{8}$$

It can be seen from Table 5 that the larger the specimen notch radius, the larger the critical equivalent plastic strain and the smaller the triaxiality. The calculated values of α and η from different notch radius specimens are very close to each other verifying that α and η are fundamental material properties indicative of toughness. The α and η values for deposit metal are the largest among the three materials, that for base metal are the second and heat affected zone the smallest. It indicates that the toughness of deposit metal is the best, that of base metal is the second and that of heat affected zone is the worst. The calibrated parameters for the three materials can be used to predict the location and the time of fracture initiation in welded steel connections.

Table 5 Calculation results of parameters α and η

Material	Notch size mm	No.	Δf (mm)	$\varepsilon_p^{critical}$	σ_e (MPa)	σ_m (MPa)	α	η
Base metal	1.5	4-1	1.17	0.44	761.34	876.29	2.45	2.70
		5-1	1.26	0.48	787.07	884.66	2.62	2.95
	3.125	10-1	1.63	0.61	852.63	745.61	2.27	2.40
		11-1	1.67	0.63	863.79	753.11	2.34	2.47
	6.25	16-1	2.38	0.79	943.77	711.04	2.43	2.37
		17-1	2.41	0.81	954.68	720.31	2.50	2.42
			Mean value				2.44	2.55
			Deviation				7%	16%
Deposit metal	1.5	4-2	1.21	0.52	771.56	860.65	2.78	3.23
		5-2	1.05	0.43	727.67	845.72	2.47	2.79
	3.125	10-2	1.59	0.61	814.26	720.60	2.29	2.45
		11-2	1.51	0.57	793.98	705.76	2.15	2.29
	6.25	16-2	2.60	0.92	967.20	755.88	2.96	2.79
		17-2	2.21	0.74	878.16	662.14	2.28	2.23
			Mean value				2.49	2.63
			Deviation				19%	23%
Heat affected zone	1.5	4-3	1.17	0.47	768.33	875.01	2.58	2.90
		5-3	1.13	0.44	751.88	870.41	2.47	2.71
	3.125	10-3	1.55	0.58	824.01	731.42	2.19	2.31
		11-3	1.59	0.59	832.01	736.98	2.24	2.37
	6.25	16-3	2.49	0.85	962.28	740.51	2.70	2.57
		17-3	2.30	0.77	921.56	697.66	2.40	2.32
			Mean value				2.43	2.53
			Deviation				11%	15%

4.4 Cyclic notched bar tests

Totally thirty-six circumferentially smooth-notched cyclic specimens made of the three materials were manufactured. The design dimensions of the cyclic specimens are the same as those of monotonic tensile specimens. Since the flat stress and strain gradients of the cyclic specimens minimize the failure dependence on characteristic length l^*, cyclic notched bar tests are feasible for the calibration of the cyclic micromechanical models. Serial numbers and measured dimensions of the specimens can be seen in Table 6. Two types of loading histories, denoted as CTF and C-PTF respectively, were used to calibrate the models for general loading histories. CTF (i.e., Cycle to Failure) involves cycling the applied displacements between two determined levels until failure

Table 6 Serial numbers and measured dimensions of the notched cyclic specimens

Material	Notch size (mm)	Loading type	No.	Loading strain (mm/mm)	Elongation (mm)	Diameter of gage length part (mm)	Diameter of notched part (mm)
Base metal	1.5	CTF	6-1	0↔0.015	0↔0.375	12.48	6.30
		CTF	7-1	0↔0.02	0↔0.5	12.48	6.26
		C-PTF	8-1	5(0↔0.01)	5(0↔0.25)	12.52	6.26
		C-PTF	9-1	5(0↔0.01)	5(0↔0.25)	12.55	6.26
	3.125	CTF	12-1	0↔0.03	0↔0.75	12.47	6.31
		CTF	13-1	0↔0.03	0↔0.75	12.50	6.28
		C-PTF	14-1	5(0↔0.015)	5(0↔0.375)	12.51	6.30
		C-PTF	15-1	5(0↔0.015)	5(0↔0.375)	12.47	6.29
	6.25	CTF	18-1	0↔0.045	0↔1.125	12.51	6.27
		CTF	19-1	0↔0.045	0↔1.125	12.50	6.30
		C-PTF	20-1	5(0↔0.025)	5(0↔0.625)	12.48	6.29
		C-PTF	21-1	5(0↔0.025)	5(0↔0.625)	12.41	6.25
Deposit metal	1.5	CTF	6-2	0↔0.02	0↔0.5	12.54	6.20
		CTF	7-2	0↔0.02	0↔0.5	12.56	6.23
		C-PTF	8-2	5(0↔0.01)	5(0↔0.25)	12.56	6.26
		C-PTF	9-2	5(0↔0.01)	5(0↔0.25)	12.51	6.16
	3.125	CTF	12-2	0↔0.03	0↔0.75	12.45	6.26
		CTF	13-2	0↔0.03	0↔0.75	12.52	6.30
		C-PTF	14-2	5(0↔0.015)	5(0↔0.375)	12.53	6.24
		C-PTF	15-2	5(0↔0.015)	5(0↔0.375)	12.49	6.20
	6.25	CTF	18-2	0↔0.045	0↔1.125	12.51	6.30
		CTF	19-2	0↔0.045	0↔1.125	12.53	6.33
		C-PTF	20-2	5(0↔0.025)	5(0↔0.625)	12.46	6.36
		C-PTF	21-2	5(0↔0.025)	5(0↔0.625)	12.57	6.28
Heat affected zone	1.5	CTF	6-3	0↔0.02	0↔0.5	12.55	6.24
		CTF	7-3	0↔0.02	0↔0.5	12.50	6.28
		C-PTF	8-3	5(0↔0.01)	5(0↔0.25)	12.54	6.24
		C-PTF	9-3	5(0↔0.01)	5(0↔0.25)	12.54	6.23
	3.125	CTF	12-3	0↔0.03	0↔0.75	12.52	6.30
		CTF	13-3	0↔0.03	0↔0.75	12.51	6.32
		C-PTF	14-3	5(0↔0.015)	5(0↔0.375)	12.54	6.21
		C-PTF	15-3	5(0↔0.015)	5(0↔0.375)	12.46	6.30
	6.25	CTF	18-3	0↔0.045	0↔1.125	12.52	6.31
		CTF	19-3	0↔0.045	0↔1.125	12.54	6.30
		C-PTF	20-3	5(0↔0.025)	5(0↔0.625)	12.48	6.15
		C-PTF	21-3	5(0↔0.025)	5(0↔0.625)	12.51	6.25

occurs, while C-PTF (i.e., Cycle and Pull to Failure) involves cycling the specimen for a finite number of cycles at lower amplitudes and then applying a tensile excursion until failure. The cyclic tests were controlled by strain. The gage length of the extensometer is 25 mm.

The force elongation curves of these specimens show a sudden loss in slope at a certain point during the last tensile cycle, and as in the case of monotonic loading, this is assumed to be the point of ductile crack initiation under cyclic loading Δ_f^{cyclic}. Δ_f^{cyclic} is recorded for use in the finite element analyses.

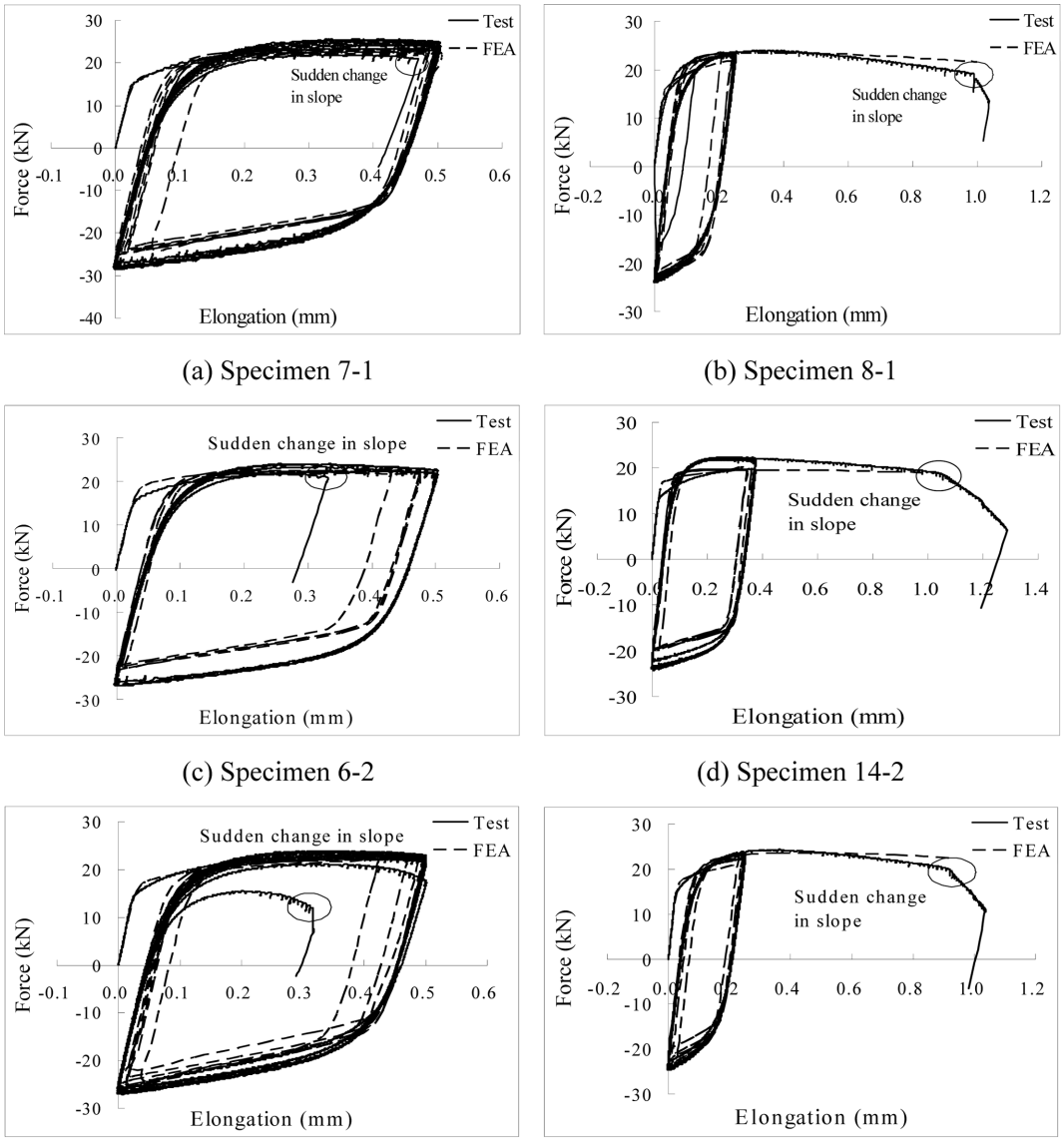

(a) Specimen 7-1 (b) Specimen 8-1

(c) Specimen 6-2 (d) Specimen 14-2

(e) Specimen 6-3 (f) Specimen 8-3

Fig. 8 Comparison of FEA and test data for force elongation curves for cyclic notched bar specimens

Cyclic finite element simulations were used to analyze notched cyclic specimens to calibrate the parameters of the DSPS and the CVGM models. The mesh for the FEM was identical to the monotonic analysis and the simulations were run on ABAQUS/CAE 6.10.

Like the monotonic analyses, the finite element solutions employed nonlinear, large deformation behavior, and cyclic plasticity. The cyclic plasticity model was based on Lemaitre-Chaboche model (Lemaitre and Chaboche 1990) and used a von Mises yield surface combining nonlinear isotropic and kinematic hardening. The material parameters in the kinematic hardening component of the model were substituted in the ABAQUS model by an array of true stresses and plastic strains. The isotropic hardening component is described by Eq. (9)

$$\sigma^0 = \sigma|_0 + Q_\infty(1 - e^{-b \cdot \varepsilon_p}) \tag{9}$$

Where the current elastic range σ^0 is defined as a function of the initial elastic range $\sigma|_0$, the equivalent plastic strain ε_p, and two model parameters are Q_∞ and b. The parameters Q_∞ and b in the isotropic hardening component were determined from a trial procedure based on achieving the best fit between the cyclic notched bar force-displacement data from the tests and the simulations.

Fig. 8 gives the comparison of finite element analyses and test data for force elongation curves for six typical specimens of the three materials. It can be seen that the FEA curves are very close to the test curves. The agreement shown here is representative of all the other specimens.

For the DSPS model, the significant plastic strain of the middle node of the specimen was

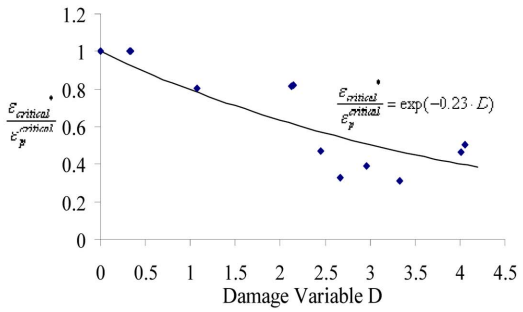

(a) Base metal

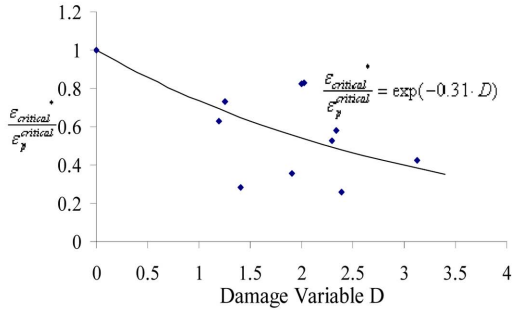

(b) Deposit metal

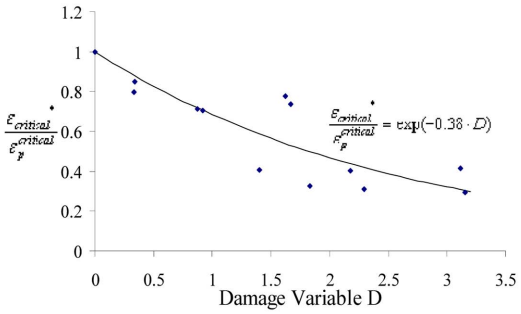

(c) Heat affected zone

Fig. 9 Scatter plots and curve fits for calibrating λ_{DSPS}

monitored leading up to failure. The final significant plastic strain value (corresponding to Δ_f^{cyclic}) was recovered as the critical significant plastic strain ε_{cyclic}^{*}. This value was then compared to the mean critical equivalent plastic strain ε_p^{cyclic} recovered from the monotonic analysis of a similar test. The ratio between the critical values of the significant and equivalent plastic strains from the cyclic and the monotonic tests represented the deterioration in the critical void ratio due to cyclic loading.

The equivalent plastic strain at the beginning of the final cycle was denoted as the damage variable D, and the damage ratio was plotted against this quantity. This process was repeated for all the tests (including the two different loading types and the three different notch sizes). Results of these analyses were summarized in scatter plots shown in the following Fig. 9. A least squares fit to the data returned the damage ratio as a function of the damage variable. An exponential function, of the type shown in Eq. (10) was chosen as the damage function:

$$f_{DSPS}(D) = \exp(-\lambda_{DSPS} \cdot D) = \varepsilon_{cyclic}^{*} / \varepsilon_p^{cyclic} \tag{10}$$

Fig. 9 shows the exponential curve fit to the scatter-data. Such a procedure returned the λ_{DSPS} value for each of the three materials. Table 7 lists the λ_{DSPS} values obtained for each of the materials from curve fitting to the scatter plots.

For the CVGM model, a similar strategy was employed, where the stress and strain histories were monitored at the middle node of the specimen until the point of failure for each test. The integrals on the right hand side of Eq. (11) were evaluated numerically at the point of failure.

$$\eta_{cyclic} = \sum_{tensile-cycles} \int_{\varepsilon_1}^{\varepsilon_2} \exp(|1.5T|) \cdot d\varepsilon_t - \sum_{compressive-cycles} \int_{\varepsilon_1}^{\varepsilon_2} \exp(|1.5T|) \cdot d\varepsilon_c \tag{11}$$

The left hand side of Eq. (11) is the cyclic demand which is to be compared to the deteriorated value of the VGM toughness index η. Thus, the damage ratio for each test can be estimated as the cyclic void growth capacity η_{cyclic} calculated in Eq. (11) at the point of failure divided by the mean value of the monotonic toughness index η.

As in the case of the DSPS model, the damage ratio was plotted against the damage variable D, which was the equivalent plastic strain at the beginning of the final or failure tensile excursion. Repeating this procedure for the different tests and doing a nonlinear regression to fit an exponential curve shown in Eq. (12) through the scatter plot can provide the value of λ_{CVGM}, as can be seen in Fig. 10. Table 7 lists the λ_{CVGM} values for each of the materials. It is shown that the values of damage degraded parameters λ_{DSPS} and λ_{CVGM} are largest for heat affected zone and smallest for base metal which indicates that in the same condition under cyclic loading, fracture initiation is easiest to take place in heat affected zone and hardest to take place in base metal. The result agrees with the research of Tateishi and Hanji (2004).

$$f_{CVGM}(D) = \exp(-\lambda_{CVGM} \cdot D) = \eta_{cyclic} / \eta \tag{12}$$

The deviation of the exponential relationship between the damage variable and the damage ratio in Eqs. (10) and (12) from the experimental data may be due to the mean values of α and η used in the calibration process. For the DSPS model, it is necessary to run a monotonic analysis of the notched round bars for the exact same geometry as the cyclic analysis and use the calibrated mean values of α to get the mean critical equivalent plastic strain $\varepsilon_p^{critical}$ which is used as the

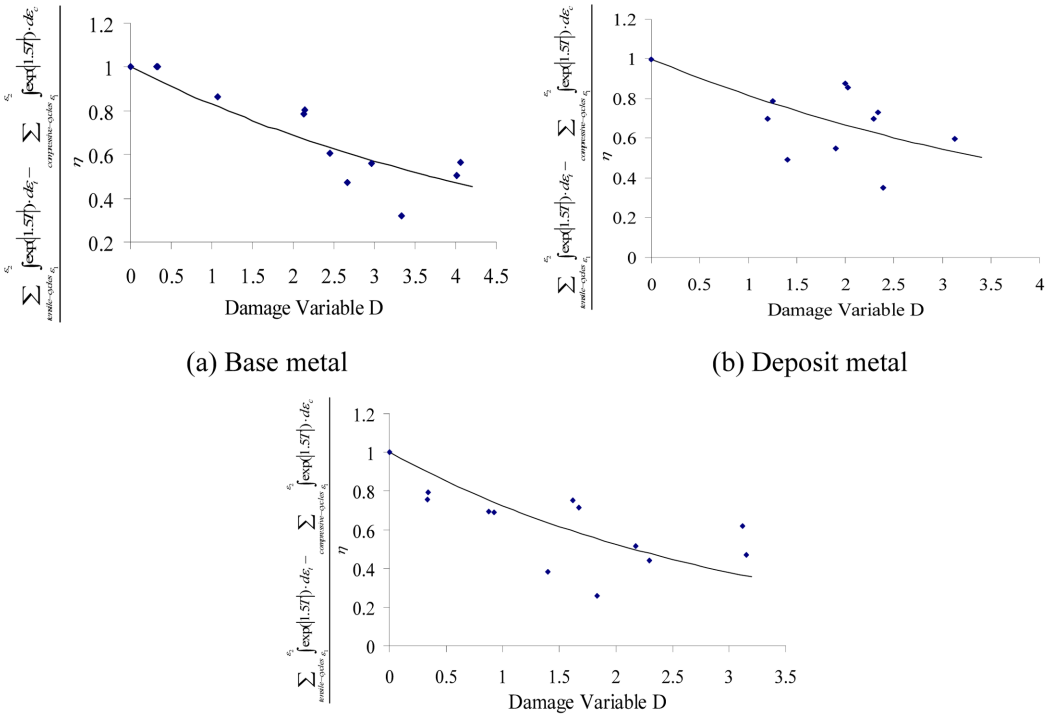

(a) Base metal (b) Deposit metal

(c) Heat affected zone

Fig. 10 Scatter plots and curve fits for calibrating λ_{CVGM}

Table 7 The λ_{DSPS} and the λ_{CVGM} values for the three different materials

Material	λ_{DSPS}	λ_{CVGM}
Base metal	0.23	0.20
Deposit metal	0.31	0.25
Heat affected zone	0.38	0.33

denominator of the damage ratio. The deviation of α shown in Table 5 may result in the deviation between the exponential relationship and the experimental data. Similarly for the CVGM model, the deviation of η may cause the deviation between the exponential relationship and the experimental data. As can be seen from Table 5, the deviations of α and η for deposit metal are the largest that may lead to the largest deviation between the exponential relationship and the experimental data. Another reason for the deviation may be the test occasionality.

4.5 Scanning electron microscope tests

The fracture surfaces of nine notched tensile specimens were scanned at a 45 degree angle to the

Fig. 11 Scanning electron microscope set-up

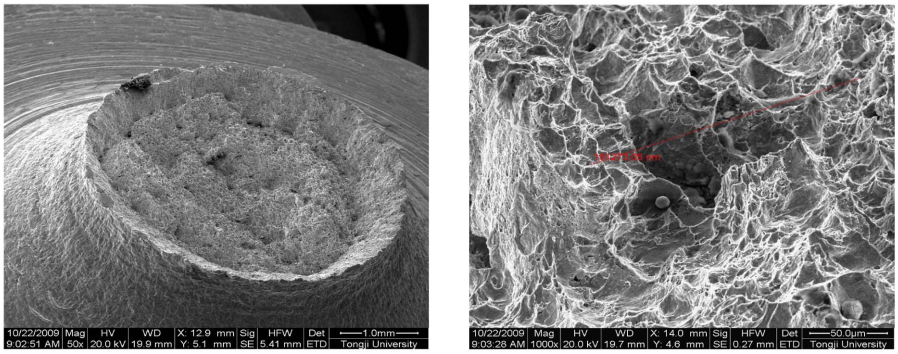

Fig. 12 Typical fracture surfaces of specimen 4-1

surfaces to measure the characteristic length l^* of the three materials. The test set-up is shown in Fig. 11.

Two bounds and a most likely value were taken for the characteristic length l^*. The typical fracture surface is shown in Fig. 12. The upper bound, lower bound and mean value of characteristic length l^* for each specimen are listed in Table 8, which shows that the mean characteristic length values for all the three materials are in the range of 0.201-0.329mm. For steel structures with high stress and strain gradients, the characteristic length significantly affects the fracture prediction. Therefore, in such circumstances, the upper bound, mean and the lower bound of l^* are used to predict three values for the point of fracture initiation to help explain some of the experiment scatter.

5. Comparison of the calibrated parameters for Q345 steel with other structural steels

In the previous research, parameters in micromechanical models of seven different batches of structural steels were calibrated (Kanvinde and Deierlein 2004). Four of them were manufactured in the United States, and three of them were manufactured in Japan. This section compares the

calibrated parameters for the three different locations of Q345 steel with that of the other seven previously calibrated structural steels. The detailed comparison can be seen in Table 9, which shows that the toughness index parameters α in the SMCS model and η in the VGM model are connected with ductility of the material indicated by the ratio of initial to final uniaxial tensile bar diameter d_0/d_f. The larger the ductility of the material, the larger the values of α and η. However, the values of α and η almost have no correlation with the yield strength, ultimate strength or the ratio of ultimate strength to yield strength. While the damage degraded parameters λ_{DSPS} in the DSPS model and λ_{CVGM} in the CVGM model and the characteristic length parameter are irrelevant with any properties of the material.

Table 8 Estimate of characteristic lengths of different specimens

Material	No.	Characteristic length (mm)		
		Lower bound	Mean value	Upper bound
Base metal	4-1	0.086	0.214	0.457
	10-1	0.107	0.177	0.311
	16-1	0.068	0.213	0.652
	Mean value	0.087	0.201	0.473
Deposit metal	4-2	0.046	0.197	0.269
	10-2	0.077	0.181	0.300
	16-2	0.063	0.228	0.365
	Mean value	0.062	0.202	0.311
Heat affected zone	4-3	0.102	0.405	0.715
	10-3	0.044	0.221	0.404
	16-3	0.070	0.361	0.893
	Mean value	0.072	0.329	0.671

Table 9 Comparison of micromechanical model parameters for different structural steels

Steel[a]	σ_y (MPa)	σ_u (MPa)	$\frac{\sigma_u}{\sigma_y}$	$\frac{d_0}{d_f}$	α	η	λ_{DSPS}	λ_{CVGM}	l^* lower (mm)	l^* mean (mm)	l^* upper (mm)
Q345BM	320.8	522.9	1.63	1.95	2.44	2.55	0.23	0.20	0.087	0.201	0.473
Q345DM	380.1	491.3	1.29	1.94	2.49	2.63	0.31	0.25	0.062	0.202	0.311
Q345HAZ	358.7	520.2	1.45	1.91	2.43	2.53	0.38	0.33	0.072	0.329	0.671
AW50	422.7	494.4	1.17	1.91	2.59	2.80	0.38	0.11	0.089	0.203	0.381
AP50	388.2	588.1	1.51	1.50	1.18	1.13	0.49	0.32	0.084	0.178	0.432
AP110	799.1	851.5	1.07	1.45	1.46	1.50	0.48	0.37	0.058	0.229	0.483
AP70HP	586.8	694.3	1.18	1.95	2.90	3.19	0.43	0.31	0.064	0.305	0.406
JP50	328.2	515.1	1.57	1.87	2.89	2.87	0.85	0.71	0.071	0.229	0.356
JP50HP	413.0	516.4	1.25	2.20	4.67	5.09	0.25	0.20	0.056	0.127	0.229
JW50	338.5	475.8	1.41	2.06	4.23	4.61	0.41	0.31	0.061	0.229	0.356

[a]Q345BM = Q345 base metal; Q345DM = Q345 deposit metal; Q345HAZ = Q345 heat affected zone; producer (A = USA; J = Japanese); rolled product (W = wide flange; P = plate); and HP = high performance bridge steel.

6. Application of calibrated micromechanical models to welded steel connection

When the above calibrated SMCS and VGM models are applied to predict fracture of welded steel connection made of Q345 steel under monotonic loading, finite element analysis of the welded steel connection is conducted, and the stress strain history of each critical point is monitored and substituted in the fracture prediction criteria Eqs. (2) and (1) of base metal, deposit metal and heat affected zone. If Eqs. (2) and (1) are satisfied over the material characteristic length l^*, then it can be predicted, according to the SMCS model and the VGM model respectively, that fracture occurs and the place of crack initiation can also be obtained.

When the calibrated DSPS model is applied to predict fracture of welded steel connection under cyclic loading, it is necessary to run a monotonic analysis prior to the cyclic tests to obtain the equivalent plastic strains at failure under monotonic loading. The critical significant plastic strain of each critical point under reversed cyclic loading is calculated according to Eq. (4). In the last tensile cycle, the difference of the actual significant plastic strain and the critical significant plastic strain $\varepsilon^* - \varepsilon^*_{critical}$ is calculated. When its value exceeds zero over the characteristic length l^*, fracture of the connection is predicted to occur.

When the calibrated CVGM model is applied to predict fracture of welded steel connection under cyclic loading, it is not necessary to run a monotonic analysis, the parameter η of VGM model can be used directly. While running the FEM simulation, the damage variable ε_p is calculated at each critical point and used to degrade the critical value of the parameter η according to the following Eq. (13)

$$\eta_{cyclic} = \exp(-\lambda_{CVGM}\varepsilon_p) \cdot \eta_{monotonic} \tag{13}$$

During the final excursion, value of $\left(\sum_{tensile-cycles} \int_{\varepsilon_1}^{\varepsilon_2} \exp(|1.5T|) \cdot d\varepsilon_t - \sum_{compressive-cycles} \int_{\varepsilon_1}^{\varepsilon_2} \exp(|1.5T|) \cdot d\varepsilon_c \right) - \eta_{cyclic}$ at each critical point is calculated. Ductile crack initiation is predicted to occur when its value exceeds zero over the characteristic length l^*.

7. Conclusions

This paper presents four kinds of tests to calibrate the parameters in micromechanics-based fracture prediction models for popularly used Q345 steel in China. The test specimens were made from base metal, deposit metal and heat affected zone to investigate crack initiation in welded connections. Results of the nine uniaxial tensile tests of round bars provide stress-strain data, elastic modulus, strength and ductility of the three materials. Parameters α and η of the monotonic models SMCS and VGM were calibrated through eighteen tensile tests of circumferentially smooth-notched bars and corresponding finite element analyses. The calibrated values of these toughness indexes show that the toughness of deposit metal is the best, that of base metal is the second and that of heat affected zone is the worst. Parameters λ_{DSPS} and λ_{CVGM} of the cyclic models DSPS and CVGM were calibrated through thirty-six cyclic tests of circumferentially smooth-notched bars, their finite element analyses and curve fitting of scatter plots. Their values are largest for heat affected zone and smallest for base metal which indicates that in the same condition under cyclic loading, fracture initiation is easiest to occur in heat affected zone and hardest to occur in base metal. The values of

characteristic length l^* of the three materials have been obtained from scanning of nine fracture surfaces. The difference of the l^* values for the three materials is not remarkable. The upper bound, mean and the lower bound of l^* were obtained for use in the high stress and strain gradient situations to help explain the experiment scatter. The calibrated parameters for the three different locations of Q345 steel were compared with that of the other previously calibrated structural steels showing that the toughness index parameters α in the SMCS model and η in the VGM model are related to the ductility of the material. The larger the ductility of the material, the larger the values of α and η. However, the values of α and η almost have no correlation with the yield strength, ultimate strength or the ratio of ultimate strength to yield strength. What's more, the damage degraded parameters λ_{DSPS} in the DSPS model and λ_{CVGM} in the CVGM model and the characteristic length parameter are irrelevant with any properties of the material. The calibrated micromechanics-based models SMCS, VGM and DSPS, CVGM can be used to predict fracture initiation of welded connections made of Q345 steel under monotonic loading and cyclic loading, respectively. Future work in this study will include the validation of these micromechanics-based fracture prediction models through large scale welded steel tubular connection tests and the establishment of fracture criteria for welded steel tubular connections.

Acknowledgements

The presented work was supported by the Ministry of Science and Technology of China, Grant No. SLDRCE09-B-02, Natural Science Foundation of China, Grant No. 51008220 and 51038008. Any opinions, findings, conclusions, and recommendations expressed in this paper are those of the writers and do not necessarily reflect the views of the sponsors. During the author's stay at University of California, Davis as a visiting student, Dr. Amit M. Kanvinde gave a lot of valuable advice for this paper. All his helps are greatly appreciated.

References

Benzerga, A.A. and Leblond, J.B. (2010), "Ductile fracture by void growth to coalescence", *Adv. Appl. Mech.*, **44**, 169-305.

Chen, T. (2007), "Extremely low cycle fatigue assessment of thick-walled steel piers", Ph.D. Thesis, Nagoya University, Japan.

Chi, W.M. (2000), "Prediction of steel connection failure using computational fracture mechanics", Ph.D. Thesis, Stanford University, CA, USA.

Fell, B.V., Myers, A.T., Deierlein, G.G. and Kanvinde, A.M. (2006), "Testing and simulation of ultra-low cycle fatigue and fracture in steel braces", *Proceedings of the 8th U.S. National Conference on Earthquake Engineering*, San Francisco, CA, USA.

Hancock, J.W. and Cowling, M.J. (1980), "Role of state of stress in crack-tip failure processes", *Meth. Sci.*, **14**(8-9), 293-304.

Hancock, J.W. and Mackenzie, A.C. (1976), "On the mechanics of ductile failure in high-strength steel subjected to multi-axial stress states", *J. Mech. Phys. Solids*, **24**(3), 147-169.

Kanvinde, A.M. and Deierlein, G.G. (2006), "Void growth model and stress modified critical strain model to predict ductile fracture in structural steels", *J. Struct. Eng.*, **132**(12), 1907-1918.

Kanvinde, A.M. and Deierlein, G.G. (2007a), "Finite-element simulation of ductile fracture in reduced section pull-plates using micromechanics-based fracture models", *J. Struct. Eng.*, **133**(5), 656-664.

Kanvinde, A.M. and Deierlein, G.G. (2007b), "Cyclic void growth model to assess ductile fracture initiation in structural steels due to ultra low cycle fatigue", *J. Eng. Mech.*, **133**(6), 701-712.
Kanvinde, A.M. and Deierlein, G.G. (2008), "Validation of cyclic void growth model for fracture initiation in blunt notch and dogbone steel specimens", *J. Struct. Eng.*, **134**(9), 1528-1537.
Kuroda, M. (2002), "Extremely low cycle fatigue life prediction based on a new cumulative fatigue damage model", *Int. J. Fatigue*, **24**(6), 699-703.
Lemaitre, J. and Chaboche, J.L. (1990), *Mechanics of Solid Materials*, Cambridge University Press.
Myers, A.T., Deierlein, G.G. and Kanvinde, A.M. (2009), "Testing and probabilistic simulation of ductile fracture initiation in structural steel components and weldments", Technical Rep. 170, John A. Blume Earthquake Engineering Center, Stanford University, CA, USA.
Panontin, T.L. and Sheppard, S.D. (1995), "The relationship between constraint and ductile fracture initiation as defined by micromechanical analyses", *Fract. Mech.*, **26**, 54-85.
Rice, J.R. and Tracey, D.M. (1969), "On the ductile enlargement of voids in triaxial stress fields", *J. Mech. Phys. Solids*, **17**(3), 201-217.
Stojadinovic, B., Goel, S.C. and Lee, K.H. (2000), "Development of post-Northridge steel moment connections", *Proceedings of the 12th World Conference on Earthquake Engineering*, New Zealand.
Tateishi, K. and Hanji, T. (2004), "Low cycle fatigue strength of butt-welded steel joint by means of new testing system with image technique", *Int. J. Fatigue*, **26**(12), 1349-1356.
Tateishi, K., Hanji, T. and Minami, K. (2007), "A prediction model for extremely low cycle fatigue strength of structural steel", *Int. J. Fatigue*, **29**(5), 887-896.
Theocaris, P.S. (1995), "Failure criteria for isotropic bodies revisited", *Eng. Fract. Mech.*, **51**(2), 239-264.